metrology

MDPI

Article

In Situ Visualization of Inhomogeneities in the Magnetic Properties of Permanent Magnets

Maximilian Lanz *, Gerhard Martinek, Gerhard Schneider and Dagmar Goll *

Materials Research Institute, Aalen University, 73430 Aalen, Germany; gerhard.martinek@hs-aalen.de (G.M.); gerhard.schneider@hs-aalen.de (G.S.)

* Correspondence: maximilian.lanz@hs-aalen.de (M.L.); dagmar.goll@hs-aalen.de (D.G.); Tel.: +49-7361-576-1601 (D.G.)

Abstract: Irreversible demagnetization processes in high-performance Fe-Nd-B magnets were investigated using a novel test rig. Designed to capture local magnetic field distributions and integral average magnetization in situ, the rig operates under field and temperature conditions similar to those found in electric motors. Validation against established techniques such as the hysteresisgraph and Hall mapper confirmed its accuracy. Furthermore, we observed the ability to detect even small variations of less than 2.5% in coercive field strength across the sample volume using field scans. The system significantly reduces measurement times from days to hours, enabling efficient in situ detection of magnetic field distributions during the whole demagnetization process.

Keywords: permanent magnet; demagnetization process; 3D Hall mapping; hysteresisgraph; Helmholtz coil

Citation: Lanz, M.; Martinek, G.; Schneider, G.; Goll, D. In Situ Visualization of Inhomogeneities in the Magnetic Properties of Permanent Magnets. *Metrology* **2024**, *4*, 506–516. https://doi.org/10.3390/metrology4030031

Academic Editor: Nicholas Sammut

Received: 16 August 2024
Revised: 11 September 2024
Accepted: 20 September 2024
Published: 22 September 2024

1. Introduction

Permanent magnet electric motors are renowned for their high torque densities and efficiencies. However, it is important to consider operational risks such as irreversible magnetization losses of permanent magnets, which are influenced by temperature, demagnetizing field, and time [1–3]. The analysis and prediction of irreversible magnetization losses are usually based on integral magnetic measurements, which determine the average magnetization from the voltage induced in coils [4,5].

Examples of integral magnetic measurements include vibrating sample magnetometry (VSM) [6], hysteresisgraph [5] and Helmholtz coil [7] measurements.

A reduction in magnetization in permanent magnets of electric motors can significantly increase electrical power consumption to maintain the mechanical output [8–11]. Additionally, higher power consumption leads to higher temperatures, resulting in additional magnetization losses in the samples [10].

Despite the insights provided by demagnetization curves, a comprehensive understanding of permanent magnet demagnetization requires the assessment of local variations.

For instance, the local distribution of magnetic fields plays a crucial role in electric motors, as it determines mechanical noise and torque ripple [11–13]. Analyzing local variations is crucial as new permanent magnet samples are increasingly tailored to their application specific field loads. This includes not only high coercive field samples, such as those produced by grain boundary diffusion (GBD) [14], as there is also a tendency in modern motor design to actually introduce materials with varying properties over the sample volume [15]. The so-called multicomponent magnets allow to save heavy rare-earth materials (especially Dy ad Tb) by specifically increasing coercivity at the magnet edges and remanence in the center of the magnet volume [16].

Magnetic field distribution including local variations can be obtained from magnetic field mappers equipped with Hall sensors [17,18].

Since integral and local measurements use different measurement systems, fully recorded demagnetization processes are time consuming. For example, in each measurement cycle, the sample is exposed to a demagnetizing field at different temperatures, followed by measurements with the Helmholtz coil and the Hall mapper after the sample has cooled down to ambient temperature. Therefore, a novel test rig has been developed. It allows measurements of the demagnetization process of samples both integrally (average magnetization) and locally (magnetic field distribution) in situ under different field and temperature conditions in a single device. This setup allows comprehensive demagnetization studies on a time scale that is difficult to achieve by ex situ methods. This paper presents the design of the test rig, a comparison with state-of-the-art equipment, and experimental results demonstrating the usefulness and reliability of this approach.

2. Materials and Methods

Design of a Test Rig for Measuring Demagnetization Processes

A. General setup

The experimental setup of the developed test rig is shown in Figure 1a. It consists of the magnetic field stage, the sample unit, and the measurement system. The magnetic field stage was constructed using a steel yoke and water-cooled coils, providing magnetic fields H_{ext} up to 1800 kA/m. The sample unit is based on a rotating disc (Figure 1b) on which permanent magnets up to 30 × 20 × 10 mm^3 can be mounted. Common sample shapes, such as rectangular blocks, cylinders, arcs, and bread loafs, can be measured, but field scans of planar surfaces are more suitable for interpretation. On this disc, the sample can be exposed to a temperature between room temperature and 200 °C by using a local heating unit with a temperature control system (see B. *Temperature Control system*). Furthermore, a Hall probe (so-called rotating Hall probe) is installed on the rotating disc to measure the surrounding magnetic field of the field stage (Figure 1b, (3)). The Hall probe was validated by comparing its measurement signals with those of a factory-calibrated Hall probe (Senis 3-axis field transducer). The measurement signals are transmitted via a slip ring from the rotating sample disc to the measurement and control system.

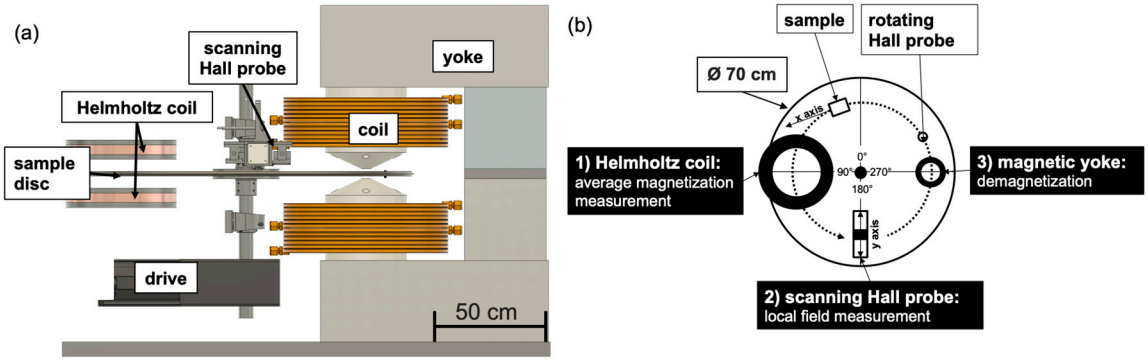

Figure 1. Setup of the developed test rig. (**a**) Overall design of the test rig with the magnetic field stage, including a magnetic yoke and coils. The measurement system consists of a Helmholtz coil for integral measurements and a scanning Hall probe for local measurements of the temperature-controlled sample on the sample disc. (**b**) Schematic overview of the rotating sample disc, highlighting static components in black and rotating objects in white. During one rotation, the sample is measured for average magnetization by the Helmholtz coil (1), scanned by the Hall probe (2), and demagnetized by the magnetic yoke (3).

The magnetic moment of the sample is determined integrally by measuring the voltage induced in the Helmholtz coil (Magnetphysik MS150) during rotation (Figure 1b, (1)). A fluxmeter (Magnetphysik EF-14) [19] integrates this voltage over time, resulting in the magnetic flux Φ, which is then used to calculate the recoil polarization J_{rec}. Both the Helmholtz coil and the fluxmeter are factory calibrated. The local measurement (Figure 1b,

(2)) employs a 3D Hall probe to capture the sample's magnetic field $B_{scan\ field}$ in the z-axis direction [10,20,21]. A motorized linear stage shifts the Hall probe along the y-axis between rotations, while an encoder tracks its angular position along the x-axis. The Hall probe (Senis SENM3Dx Field Transducer) is a factory-calibrated 3D Hall probe with a maximum magnetic resolution of 1×10^{-6} T and temperature compensation from -40 to 125 °C. This scanning Hall probe allows 2D scans of the magnetic field over multiple rotations, which is represented in MATLAB in the top $B_z(x, y)$, front $B_z(y, z)$ and side $B_z(x, z)$ views (Figure 2b).

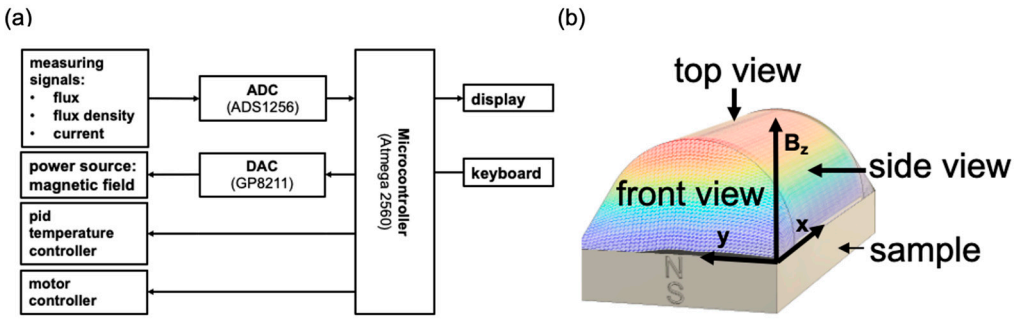

Figure 2. (**a**) Schematic overview of the measuring and control setup. (**b**) Illustration of the sample coordinate system and different projections of the magnetic field in top, front, and side view.

The analog measurement signals of the fluxmeter and Hall probe are converted by a 24-bit analog–digital-converter (Texas Instruments ADS1256) and transferred to an Arduino microcontroller [22,23], which also controls the fluxmeter, field source and sample disc rotation (Figure 2a).

During one full sample rotation (0°–360°), the sample undergoes the following three stages:

- Helmholtz coil measurement at 90° (Figure 3, red): measurement of the average magnetization of the sample.
- Field scanning at about 180° (Figure 3, blue): mapping of the magnetic field over the sample surface.
- Demagnetizing field measurement at 270° (Figure 3, green): exposure of the sample to a demagnetizing field of the field stage, measured by the rotating Hall probe on the sample disc.

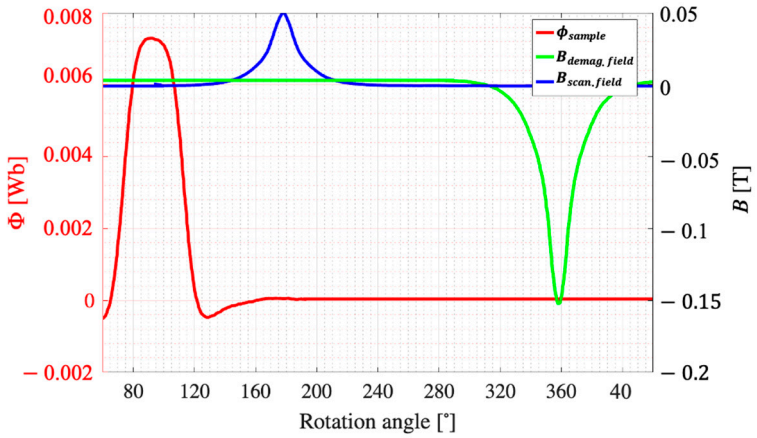

Figure 3. Measuring signals during one full sample rotation (0°–360°). Helmholtz coil flux (magnetic flux ϕ (red), position: 90°); scanning Hall probe ($B_{scan\ field}$ (blue), position: 180°); demagnetization field ($B_{demagnetizing\ field}$ (green), position: 270°).

B. Temperature Control System

The sample temperature is controlled and measured by thermocouples on both sides of the heating unit. Initial tests with several thermocouples attached to a sample body showed a uniform temperature over the sample volume. An infrared (IR) sensor (GY-904) mounted next to the Hall probe of the scanner allows us to further measure the IR emission from the sample surface, resulting in thermal maps of the temperature distribution [10]. The IR temperature measurement accuracy is ensured by applying Kapton tape with an emissivity of 0.95 to the sample surface according to [10]. The thermal map in Figure 4 shows a uniform temperature of approximately 80 °C in the central sample area (black box). The position of the heating unit is also shown (shaded areas).

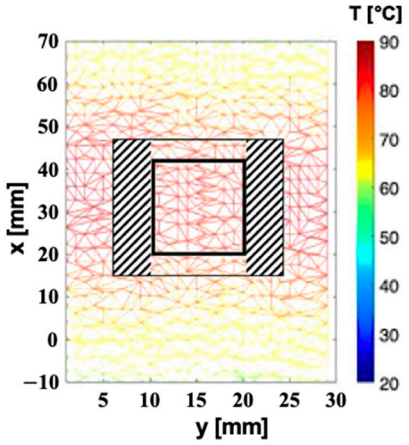

Figure 4. Temperature distribution (top view) recorded by an IR sensor at a nominal temperature of 80 °C. The positions of the sample (black box) and of the heating unit (shaded areas) are indicated.

C. Measuring Procedure

Measurements were performed on two types of Fe-Nd-B permanent magnet samples (Figure 5): an N52-SH magnet of geometry 20 × 10 × 5 mm^3, and N52-UH segmented magnet, consisting of two segments with a total geometry of 23 × 12 × 6 mm^3.

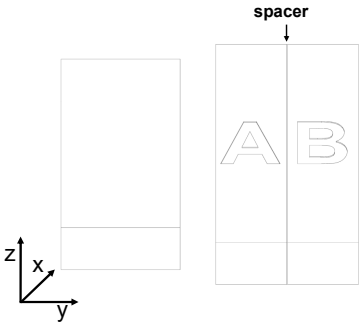

Figure 5. Illustration of the standard-grade (1 segment) N52-SH (**left**) and the N52-UH segmented sample based on segment A and B (**right**).

A sample temperature of 80° was chosen to allow measurements in the second and third quadrants of the hysteresis curves of both samples with the available applied field of 1800 kA/m. The intrinsic coercivity H_{cj} of the chosen magnets amounts to 1011 kA/m (N52-SH) and 1350 kA/m (N52-UH) at 80 °C, respectively. To minimize the effects of heat transfer from the heated sample to the scanning Hall probe, a distance of 5 mm was chosen between the sample and the active area of the Hall probe. The procedure begins by fully magnetizing the samples using a 7 T pulse magnetizer. Next, the sample is mounted on the sample disc and heated to the chosen temperature. The subsequent steps are as follows.

1. Position the sample at 0° away from the Helmholtz coil and reset the fluxmeter.
2. Measure the magnetic recoil polarization using the integral measurement system.
3. Rotate the sample while applying an external demagnetization field H_{ext} from the field stage.
4. Record the field distributions during one rotation as an x-axis line scan at $H_{ext} = 0$ using the local measurement system.
5. Repeat step 3 for 30 cycles, incrementing the y-direction of the scanner's Hall probe by one step after each cycle.

This procedure (steps 1–5) takes about 5 min and is typically repeated for 20 cycles, increasing the demagnetizing field each time, to capture the demagnetization behavior of the sample across the entire demagnetization curve.

3. Results and Discussions

3.1. Validation of the Measurement Setup

To validate the new test rig, comparisons were made with state-of-the-art measurement techniques, including a hysteresisgraph and a 3D Hall mapper, using the non-segmented N52-SH sample.

3.1.1. Demagnetization Curves in Comparison with Conventional Hysteresisgraph Measurements

Figure 6 shows the demagnetization curve of an N52-SH sample at 80 °C measured with the magnetically closed circuit hysteresisgraph (Permagraph, Magnet-Physik GmbH, Figure 6a) and open-circuit test rig (Figure 6b, red). It can be seen that the test rig shows reasonable polarization levels (J_{rec} of 1.28 T (test rig) to J_r of 1.32 T (hysteresisgraph)) and good agreement in the intrinsic coercive field, where J is close to zero (H_{cj} of −1002 kA/m (test rig) to H_{cj} of −1011 kA/m (hysteresisgraph)). The curves in Figure 6 are different due to the different measurement methods, where the closed-circuit hysteresisgraph measures $J(H_{int})$, while the open-circuit test rig measures the recoil polarization $J_{rec}(H_{ext})$ in the absence of the demagnetizing field. A rough determination of intrinsic material properties is possible by adjusting the $J_{rec}(H_{ext})$ curve (Figure 6b, red) to $J(H_{int})$ (Figure 6b, black) using an average demagnetization factor ($N = 0.49$) [24] for H and an estimated recoil permeability ($\mu_r = 0.03$) for J. However, the primary goal of this setup is to show inhomogeneities rather than a precise reproduction of the demagnetization curves.

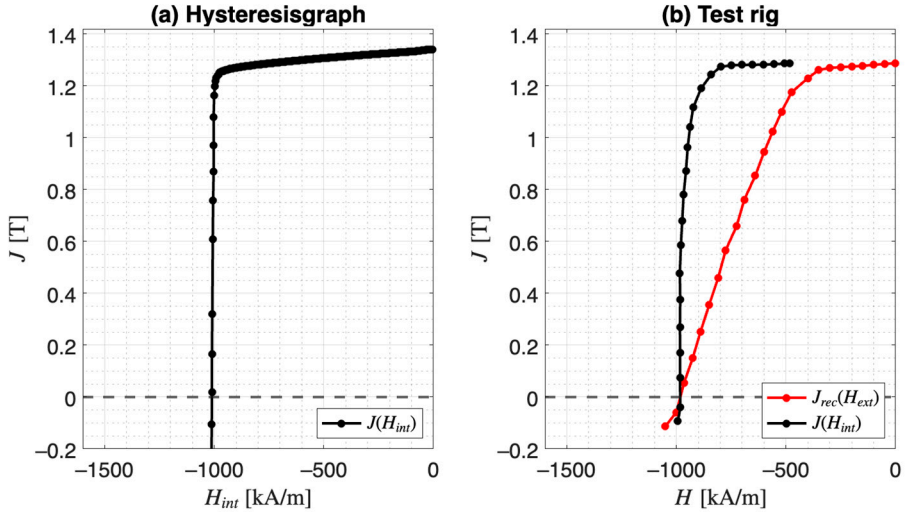

Figure 6. Demagnetization curve of the N52-SH sample at 80 °C. (**a**) Hysteresisgraph measurement (H_{cj}: −1011 kA/m). (**b**) Test rig measurement (H_{cj}: −1002 kA/m).

3.1.2. Magnetic Field Scans in Comparison with Conventional Scans

For validation, the N52-SH sample was scanned at room temperature using the newly developed test rig and a state-of-the-art 3D Hall mapper (Senis AG, Baar (Zug), Switzerland) as a reference measurement, as shown in Figure 7. The test rig map was measured with a significantly lower horizontal resolution. A lower horizontal resolution was generally applied to limit the measuring time to around 5 min per scan and thus minimize significant time-dependent losses occurring during a scan at elevated temperatures. The magnetic field measurements show comparable results for both systems, with peak values at around 120 mT and similar field distributions for the test rig and the commercial 3D Hall mapper. Figure 7 shows that the essential characteristics of the magnetic field were effectively captured by the test rig.

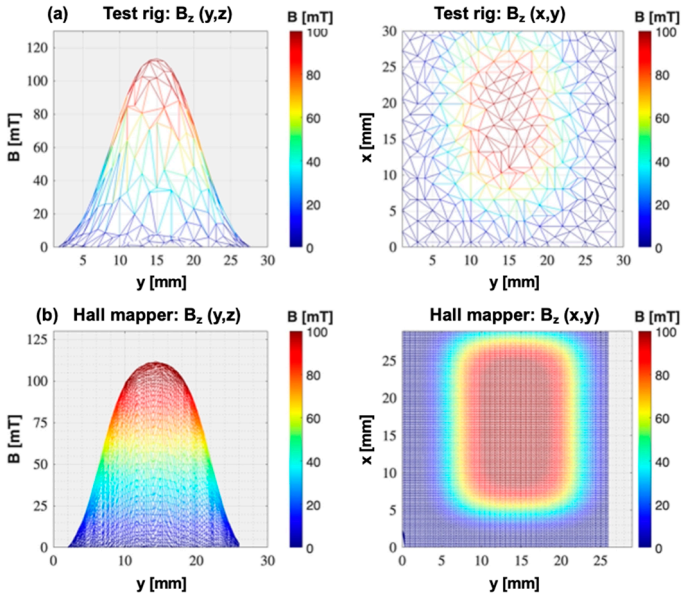

Figure 7. Magnetic field visualization of the N52-SH sample at room temperature in front view $B_z(y,z)$ and top view $B_z(y,x)$: (**a**) test rig; (**b**) Senis 3D Hall mapper (state-of-the-art).

3.2. Demagnetization Study Examples

The results of the measurements are shown in two series of plots. Each series consists of a plot of the demagnetization curve (quasi-hysteresis curve ($J_{rec} - H_{ext}$)) with labels indicating the position where selected field plots were recorded. The corresponding field plots are then presented in the front view and top view. The color distribution of the field scans was chosen to clearly show the field distributions around the sign change, with the color map limited to ± 10 mT. Signals above 10 mT appear in red, while signals below -10 mT appear in blue. The first set of measurement results shows the demagnetization of the non-segmented N52-SH sample. Figure 8 shows the quasi-hysteresis curve, indicating the magnetization states where field plots are presented in Figure 9. States (a–c) (H_{ext} : from -520 to -930 kA/m) illustrate the demagnetization in quadrant 2; state (d) represents the state near the coercive field of about -980 kA/m, followed by magnetization in the opposite direction in quadrant 3 (states (e), (f) with H_{ext} from -1050 to -1190 kA/m). The corresponding series of magnetic field distributions in Figure 9 shows a consistently uniform field peak, which gradually decreases as the demagnetizing field increases (states (a), (b), (c)). This behavior can also be observed in the top views, which decrease uniformly as the demagnetizing field increases. In states (d–f), the peak uniformly increases again with the opposite sign.

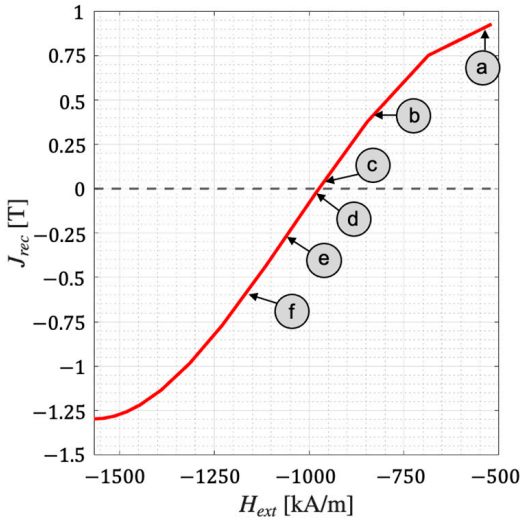

Figure 8. Demagnetization curve ($J_{recoil} - H_{ext}$) of the N52-SH sample at 80 °C with marked magnetization states for corresponding field plots in Figure 9. The following demagnetizing field strengths labelled H_{ext} [kA/m] are used: (**a**) −520, (**b**) −810, (**c**) −930, (**d**) −980, (**e**) −1050; (**f**) −1190.

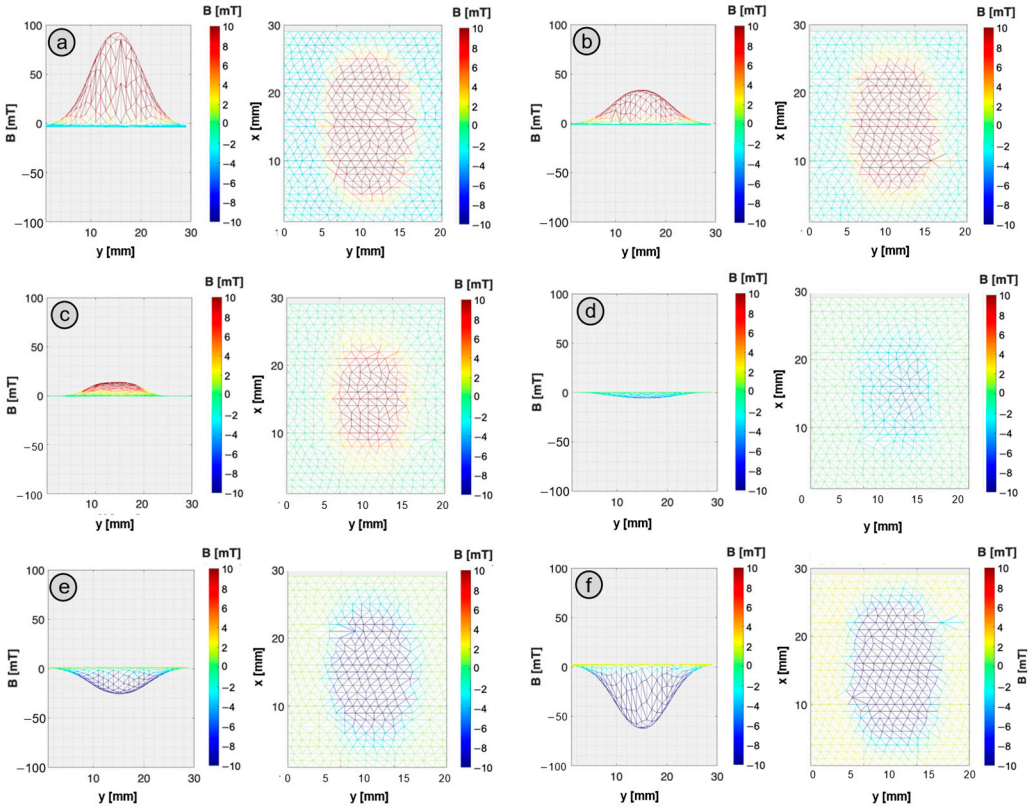

Figure 9. (**a**–**f**) Series of field visualizations corresponding to the magnetization states in Figure 9 for the non-segmented sample N52-SH at 80 °C. (**Left**) side view ($B_z(y,z)$); (**right**) top view ($B_z(y,x)$). The following demagnetizing field strengths labelled H_{ext} [kA/m] are used: (**a**) −520, (**b**) −810, (**c**) −930, (**d**) −980, (**e**) −1050; (**f**) −1190.

The second series of measurements focuses in detail on the coercivity region of the segmented sample N52-UH. This is shown in Figure 10. The quasi-hysteresis curve (states (a–e)) with H_{ext} from −1225 to −1330 kA/m illustrates the demagnetization in quadrant 2 leading to a coercive field of about −1330 kA/m (state (e)) and the magnetization in opposite direction in quadrant 3 (states (f–h) with H_{ext} from −1335 to −1350 kA/m). The

corresponding field plots are shown in Figure 11. For moderate demagnetizing fields up to state (a), only a slight, uniform demagnetization is observed, similar to the non-segmented sample. However, for state (b), the first indications of non-uniform magnetization appear along the *y*-axis. At state (c), there is an uneven demagnetization where one side (segment A) is magnetized in the opposite direction while the other side of the sample (segment B) remains magnetized in the original direction. This behavior continues up to the coercive field, where the peak values of the two segments reach an approximate equilibrium between oppositely magnetized and demagnetized values, as observed at state (e). During states (f–h), segment B also undergoes magnetization in the opposite direction.

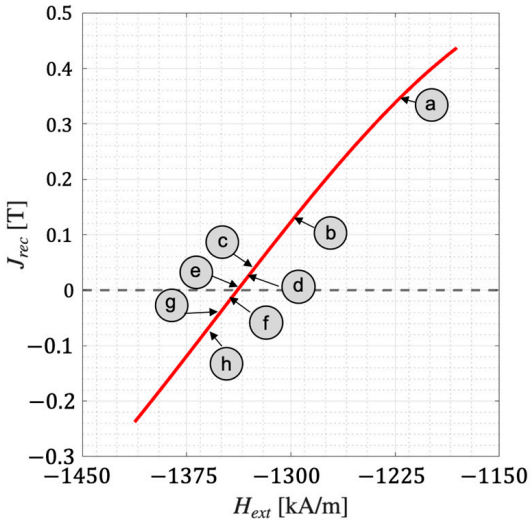

Figure 10. Demagnetization curve ($J_{rec} - H_{ext}$) of the N52-UH sample at 80 °C with magnetization states (marked) for corresponding field plots in Figure 12. The following demagnetizing field strengths labelled H_{ext} [kA/m] are used: (**a**) −1225, (**b**) −1300, (**c**) −1320, (**d**) −1324, (**e**) −1330, (**f**) −1335, (**g**) −1340; (**h**) −1350.

The non-uniform demagnetization behavior observed in the segmented sample near the coercive field suggests different coercive fields in the two segments as a possible reason. This variation in coercivity could be either due to temperature gradients in the sample or due to differences in the magnetic properties of the two segments. However, the measurements of the temperature distribution, as explained in Section II, C, did not support the first explanation. In order to identify differences in the material properties between the two segments, the segments were separated at their bond line after applying a temperature of approximately 400 °C. The magnetic properties of the two segments were then measured individually in the hysteresisgraph. Figure 12 shows that segment A has a measured coercivity of −1321 kA/m, while segment B has a coercivity of −1357 kA/m. The observed variation of around 30 kA/m (2.5% of coercive field strength) is in line with measurements from 10 other samples of the same quality, which also demonstrate variances within the range of 30 to 70 kA/m. Variations of this magnitude are not uncommon, as evidenced by manufacturer data sheets [25,26]. These data sheets typically provide a minimum value for the intrinsic coercive field strength, rather than specifying narrow limits, in contrast to other parameters. These measurements demonstrate that the equipment is capable of detecting local differences in coercivity using the in situ scanning Hall probe of the test rig and the entire demagnetization setup.

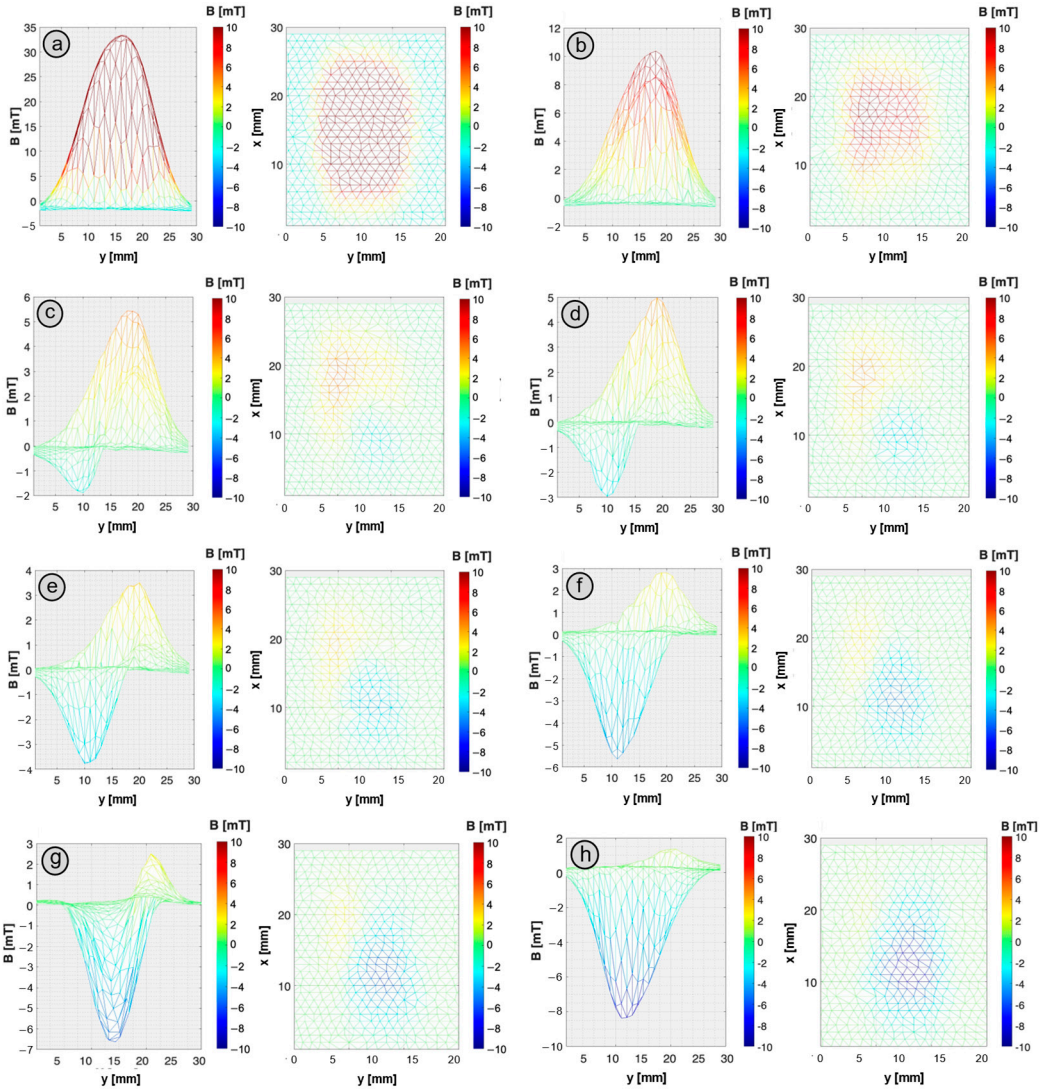

Figure 11. (**a**–**h**) Series of field visualizations corresponding to the magnetization states in Figure 11 for the segmented sample N52-UH at 80 °C. Left: side view ($B_z(y,z)$); right: top view ($B_z(y,x)$). The following demagnetizing field strengths labelled H_{ext} [kA/m] are used: (**a**) −1225, (**b**) −1300, (**c**) −1320, (**d**) −1324, (**e**) −1330, (**f**) −1335, (**g**) −1340; (**h**) −1350.

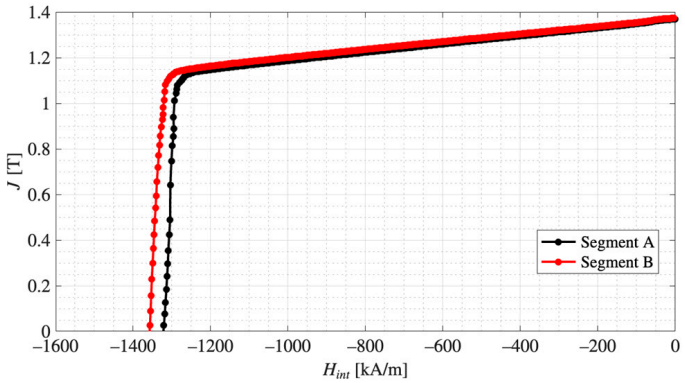

Figure 12. The demagnetization curve of segments A and B of the segmented N52-UH sample at 80 °C, measured using the hysteresisgraph, with coercive field strengths of −1321 kA/m for segment A and −1357 kA/m for segment B.

4. Conclusions

The test rig was successfully designed and implemented. The fully automated system effectively identified and visualized magnetization states induced by temperature and demagnetizing field.

Validation measurements for several Fe-Nd-B samples demonstrated good agreement between the test rig measurements and established state-of-the-art techniques, including the Hall mapper and hysteresisgraphs. The equipment can also be useful for other materials like Co-Sm and hard ferrite. As the demagnetization risk of ferrites is higher at lower temperatures, the sample heating unit should be expanded to allow cooling as well.

By analyzing different samples, we observed inhomogeneous field distributions near the coercive fields with variations of less than 30 kA/m, confirmed by single hysteresisgraph measurements. These results validate the novel measurement setup, which reduces the time for a series of demagnetization studies from days to hours. A single study now takes about five minutes, compared to nearly an hour required by the manual procedure involving heating, demagnetizing by field pulse, cooling, and measuring with a Helmholtz coil and Hall mapper. Due to the increased efficiency in time and measurement accuracy, the understanding of locally distributed irreversible magnetization changes in standard and segmented samples, such as those used in electric motors and specialized actuators, continues to grow. This enhanced understanding supports better optimization and long-term performance of permanent magnets in use.

Author Contributions: Conceptualization, M.L., G.M., G.S. and D.G.; methodology, M.L., G.M. and D.G.; hard- and software realization, M.L.; validation, M.L., G.M. and D.G.; formal analysis, M.L. and G.M.; investigation, M.L. and G.M.; resources, G.S. and D.G.; data curation, M.L.; writing—original draft preparation, M.L., G.M., G.S. and D.G.; writing—review and editing, M.L., G.M., G.S. and D.G.; visualization, M.L.; supervision, G.M., G.S. and D.G.; project administration, D.G.; funding acquisition, G.S. and D.G. All authors have read and agreed to the published version of the manuscript.

Funding: The research was funded by the Federal Ministry of Education and Research (BMBF), Germany, within the scope of the project MAGproof (grant no. 13FH116PX8). Publication funded by Aalen University of Applied Sciences.

Data Availability Statement: Data are contained within the article.

Conflicts of Interest: The authors declare no conflicts of interest.

References

1. Street, R.; Woolley, J.C. A Study of Magnetic Viscosity. *Proc. Phys. Soc. Sect. A* **1949**, *62*, 562. [CrossRef]
2. Néel, L. Le traînage magnétique. *J. Phys. Radium* **1951**, *12*, 339–351. [CrossRef]
3. Crew, D.C.; McCormick, G.; Street, R. Measurement of Magnetic Viscosity in NdFeB. *IEEE Trans. Magn.* **1996**, *32*, 4356–4358. [CrossRef]
4. Egorov, D.; Petrov, I.; Pyrhönen, J.J.; Link, J.; Stern, R.; Sergeant, P.; Sarlioglu, B. Hysteresis Loss in NdFeB Permanent Magnets in a Permanent Magnet Synchronous Machine. *IEEE Trans. Ind. Electron.* **2022**, *69*, 121–129. [CrossRef]
5. Möwius, S.; Kropff, N.; Velicescu, M. Measurement Technologies for Permanent Magnets. *Acta IMEKO* **2019**, *7*, 15. [CrossRef]
6. Foner, S. Versatile and Sensitive Vibrating-Sample Magnetometer. *Rev. Sci. Instrum.* **1959**, *30*, 548–557. [CrossRef]
7. Carnegie, D.W.; Timpf, J. Characterizing Permanent Magnet Blocks with Helmholtz Coils. *Nucl. Instrum. Methods Phys. Res. Sect. Accel. Spectrometers Detect. Assoc. Equip.* **1992**, *319*, 97–99. [CrossRef]
8. Sebastian, T. Temperature Effects on Torque Production and Efficiency of PM Motors Using NdFeB Magnets. *IEEE Trans. Ind. Appl.* **1995**, *31*, 353–357. [CrossRef]
9. Bilgin, O.; Kazan, F.A. The Effect of Magnet Temperature on Speed, Current and Torque in PMSMs. In Proceedings of the 2016 XXII International Conference on Electrical Machines (ICEM), Lausanne, Switzerland, 4–7 September 2016; IEEE: Lausanne, Switzerland, 2016; pp. 2080–2085.
10. Peng, P.; Zhang, J.; Li, W.; Leonardi, F.; Rong, C.; Degner, M.; Liang, F.; Zhu, L. Temperature-Dependent Demagnetization of Nd-Fe-B Magnets for Electrified Vehicles. In Proceedings of the 2019 IEEE International Electric Machines & Drives Conference (IEMDC), San Diego, CA, USA, 12–15 May 2019; pp. 2056–2062.
11. Ruoho, S.; Kolehmainen, J.; Ikaheimo, J.; Arkkio, A. Interdependence of Demagnetization, Loading, and Temperature Rise in a Permanent-Magnet Synchronous Motor. *IEEE Trans. Magn.* **2010**, *46*, 949–953. [CrossRef]

12. Zhu, M.; Hu, W.; Kar, N. Acoustic Noise Based Uniform Permanent Magnet Demagnetization Detection in SPMSM for High-Performance PMSM Drive. *IEEE Trans. Transp. Electrif.* **2017**, *4*, 303–313. [CrossRef]
13. Zhu, M.; Hu, W.; Kar, N. Torque Ripple Based Interior Permanent Magnet Synchronous Machine Rotor Demagnetization Fault Detection and Current Regulation. *IEEE Trans. Ind. Appl.* **2016**, *53*, 2795–2804. [CrossRef]
14. Chen, F. Recent Progress of Grain Boundary Diffusion Process of Nd-Fe-B Magnets. *J. Magn. Magn. Mater.* **2020**, *514*, 167227. [CrossRef]
15. Ucar, H.; Parker, D.S.; Nlebedim, I.C.; McCallum, R.W.; McCall, S.K.; Parans Paranthaman, M. Strategic Coating of NdFeB Magnets with Dy to Improve the Coercivity of Permanent Magnets. *Adv. Mater. Res.* **2015**, *4*, 227–233. [CrossRef]
16. Tomše, T.; Tremelling, D.; Kessler, R.; Christen, T.; Scherf, L.; Simon, R.A.; Greuter, F.; Herrmann, L.; Dubois, J.-M.; Kobe, S.; et al. Multicomponent Permanent Magnets for Enhanced Electrical Device Efficiency. *J. Magn. Magn. Mater.* **2020**, *494*, 165750. [CrossRef]
17. Blagojevic, M.; Mancic, D. The System for Magnetic Field Mapping Based on the Integrated 3D Hall Sensor. In Proceedings of the 2016 24th Telecommunications Forum (TELFOR), Belgrade, Serbia, 22–23 November 2016; pp. 1–8.
18. Bending, S.; Oral, A. Hall Effect in a Highly Inhomogeneous Magnetic Field Distribution. *J. Appl. Phys.* **1997**, *81*, 3721–3725. [CrossRef]
19. Hilzinger, R.; Rodewald, W. *Magnetic Materials: Fundamentals, Products, Properties, and Applications*; Publicis: Paris, France; VAC, Vacuumschmelze: Erlangen/Hanau, Germany, 2013; ISBN 978-3-89578-352-4.
20. Xiong, H.; Zhang, J.; Degner, M.W.; Rong, C.; Liang, F.; Li, W. Permanent-Magnet Demagnetization Design and Validation. *IEEE Trans. Ind. Appl.* **2016**, *52*, 2961–2970. [CrossRef]
21. Kaleta, J.; Wiewiórski, P. Magnetovisual Method for Monitoring Thermal Demagnetization of Permanent Magnets Used in Magnetostrictive Actuators. *J. Rare Earths* **2014**, *32*, 236–241. [CrossRef]
22. Itterheimová, P.; Foret, F.; Kubáň, P. High-Resolution Arduino-Based Data Acquisition Devices for Microscale Separation Systems. *Anal. Chim. Acta* **2021**, *1153*, 338294. [CrossRef] [PubMed]
23. Mulyono, A.E.; Mustika, T.; Sulaikan, H.P.; Kartini, E. Development of Battery Performance Data Acquisition System for Monitoring Battery Performance inside Solar Cell System. *IOP Conf. Ser. Mater. Sci. Eng.* **2018**, *432*, 012057. [CrossRef]
24. Aharoni, A. Demagnetizing Factors for Rectangular Ferromagnetic Prisms. *J. Appl. Phys.* **1998**, *83*, 3432–3434. [CrossRef]
25. Arnold Magnetic Technologies Corp. *Datasheet NdFeB, G52-UH*; Rev. 210607; Arnold Magnetic Technologies Corp.: Rochester, NY, USA, 2021.
26. VACUUMSCHMELZE GmbH & Co. KG. *Datasheet VD801DTP*; VACUUMSCHMELZE GmbH & Co. KG: Hanau, Germany, 2023.